

# Finite Element and Kinematics Analysis of Paper-Plastic Handling Dual-arm Robot

Zhizhong Lv, Ke Li, Yuanran Gong, Liang Ge, Tan Long

Nanchong key laboratory of robot engineering and intelligent manufacturing, southwest petroleum university, Chengdu, Sichuan 610000, China

## Abstract

According to the existing paper-plastic hot-pressing machine, a dual-arm robot that can move up and down and quickly transport paper and plastic is designed. Firstly, the finite element static analysis is carried out on the big arm, forearm and ball screw lifting mechanism of the dual-arm robot, and the simulation analysis is carried out in ANSYS Workbench to find the maximum deformation and maximum stress value of the three components. meet the design requirements. Then the kinematics analysis of the whole robot is carried out according to the theory of robot kinematics. Here, the improved Denavit-Hartenberg (DH) method is used to model and analyze the connecting rod of the robot, and the forward kinematics model of the robot is obtained, and then the inverse kinematics model is obtained by solving each joint through the known end pose equation. . Then, the correctness of the forward and inverse kinematics mathematical model is verified by MATLAB-Robotic Toolbox and programming. At the same time, the Monte Carlo method is used to solve the motion space of the robot's arms in MATLAB, and finally the motion of the robot is planned and simulated to verify the motion stability of the robot.

## Keywords

Dual-arm robot; finite element analysis; forward and inverse kinematics; workspace analysis.

## 1. Introduction

With the continuous development of the times, the demand for robots in all walks of life is increasing. Especially in the paper and plastic manufacturing industry, due to the requirements of the work content, it is necessary to carry out continuous handling and transfer of paper and plastic. Because the size of the hot-pressing shaping machine is different, it is necessary to consider the limitation of the hot-pressing shaping machine on the handling of the paper-plastic when the paper-plastic is hot-pressed. At the same time, considering that most robots cannot work in the case of power failure, and considering the efficiency of the robot, the designed robot can also rely on humans to operate the robot to perform normal work in the event of a power failure to complete the paper-plastic process. Uninterrupted handling, so a dual-arm robot is designed that can both work in place of humans and work in the event of a power outage.

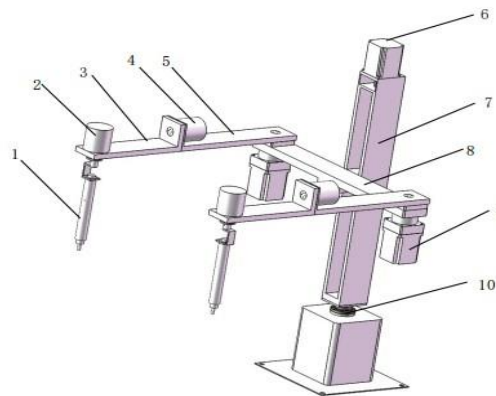
According to the use of robots with different numbers of robotic arms, they can be divided into the following categories: humanoid service arm robots, picking arm robots, rehabilitation training arm robots and underwater arm robots. Among them, the German Aerospace Center released an Albert HUBO robot [1]. This robot adopts a modular approach to design a mechanical arm, and assembles a motor, a reducer, a controller, a safety brake, and a sensor inside the arm. The robot can perform some more complex tasks through the coordination and cooperation of its two arms, such as dancing, carrying goods, tightening bottle caps, and making tea. The Eca robotics series of robots [2] produced by a French company are driven by motors. In order to

adapt to different work requirements, two different types of robotic arms with 5 functions and 7 functions are designed. Harbin Institute of Technology has developed a bionic service robot called Talos [3]. The robot is 0.6 meters tall and has 22 degrees of freedom. In order to enable the robot to take some light objects, the designer makes each palm of Both have 3 fingers.

In this paper, a dual-arm robot is designed for the handling environment of paper and plastic, and the finite element static analysis of the robot is carried out. Then, the link coordinate system of the manipulator is established according to the DH method, and the forward and inverse kinematics mathematical model of the manipulator is derived based on the principles of robotics, and the analytical solution and Jacobian matrix of the inverse kinematics are solved. The work of the manipulator is simulated by MATLAB. Space and verify the correctness of the forward and inverse kinematics model and the stability of the trajectory motion of the robotic arm.

### 2. Robot structure design

The overall structure of the robot is shown in Figure 2-1. It consists of two mechanical arms, a body ball screw lifting mechanism, a body rotating mechanism, a servo motor, an end cylinder and a suction cup. After the end suction cup of the robot absorbs the paper and plastic, it can be transported in three-dimensional space by using the mechanical arms and the fuselage rotating mechanism; at the same time, if the paper and plastic are placed in a low position, the overall mechanical arm can be moved through the fuselage ball screw. lift. The joints 1 and 2 of the wrist and forearm are composed of servo motors, and the joints of the big arm are composed of servo motors and planetary reducers; the body rotation mechanism is driven by servo motors and harmonic reducers.



1-Cylinder; 2-Wrist rotary motor; 3-Robot arm 1 (small arm); 4-Robot arm 1 rotary motor; 5-Robot arm 2 (big arm); 6-Ball screw drive motor; 7-Ball ball Lead screw; 8-Robot arm 3; 9-Robot arm 1 rotary motor; 10-Base rotary joint (harmonic reducer)

Figure 2-1 Robot structure diagram

### 3. Statics Finite Element Analysis of Robots

When the boom rotates, it is easy to deform, which shortens the mission life of the boom. Therefore, a static analysis of the boom is required. The material used for robotic arm 2 (big arm) is 1060-H12 aluminum alloy, and the material properties set in ANSYS are shown in Table 1:

Material	Mass density	Elastic Modulus	Poisson's ratio	Yield Strength
1060-H12	2700kg / m <sup>3</sup>	6.9e + 04MPa	0.33	75MPa

Fig. 1 Material properties of arm

Import the robotic arm 2 (big arm) into ANSYS Workbench, set the material parameters, and create a mesh. The mesh effect after the division is completed is shown in Figure 2-2. The average mesh quality is 0.72093, which is higher than The lowest value for grid computing is 0.7.

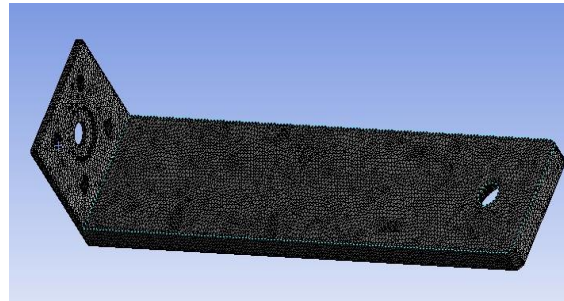


Figure 2-2 Boom meshing diagram

The A side is connected with the robotic arm 2 (big arm), which is regarded as the force-bearing surface, and the B and C sides are fixedly connected with the planetary reducer, which is regarded as the fixed support surface. The weight of the robot arm 2 (big arm) and other parts and the weight of the full load is 7.86kg. These weights are fully loaded on the A surface, so the force on the A surface is about 77N, and the direction of the force is the z-axis. negative direction.

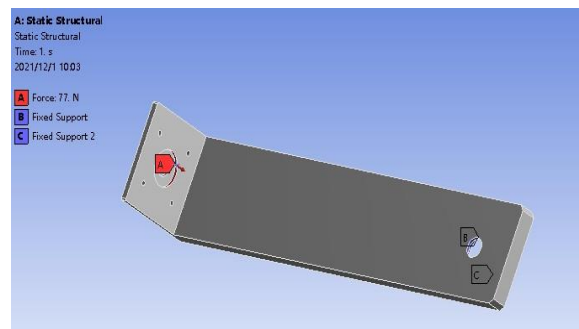


Figure 2-3 Schematic diagram of the force of the boom

After the ANSYS simulation calculation is completed, the overall deformation cloud map and equivalent stress cloud map of the robotic arm 2 (big arm) are obtained, as shown in Figures 2-4 and 2-5:

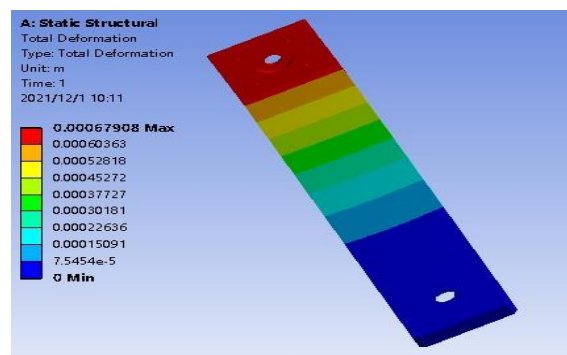


Figure 2-4 Cloud map of overall deformation of the boom

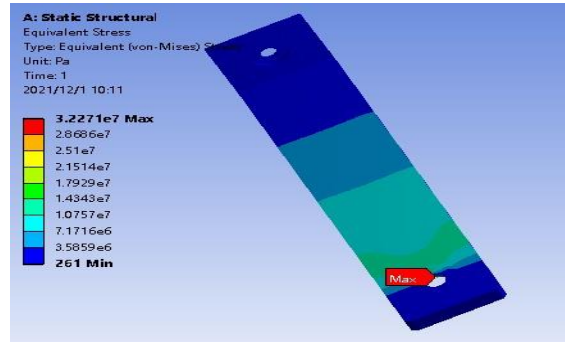


Figure 2-5 Equivalent stress cloud diagram of the boom

According to the simulation analysis results in Figure 2-4, the main deformation of the robotic arm 2 (big arm) is the force-bearing surface A, and its maximum deformation is 0.0006mm, which is very small for the overall structure, so Deformation can be ignored here. Then according to Figure 2-5, the maximum equivalent stress of robotic arm 2 (big arm) occurs at the edge of the hole, and its maximum equivalent stress is 32MPa, which is less than the yield strength of aluminum alloy 75MPa. Meet the design requirements.

The material and meshing of robotic arm 1 (small arm) are the same as those of robotic arm 2 (big arm), so the meshing diagram of robotic arm 1 (small arm):

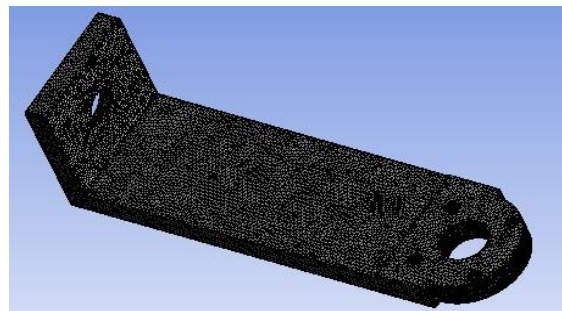


Figure 2-6 Forearm meshing diagram

Surface A is the force-bearing surface, and surfaces B and C are fixed surfaces. When the load is fully loaded, the total weight of the load and the connector is about 6kg, all of which are loaded on the A surface, so the force on the A surface is 58.8N, the direction of the force is the negative direction of the z-axis.

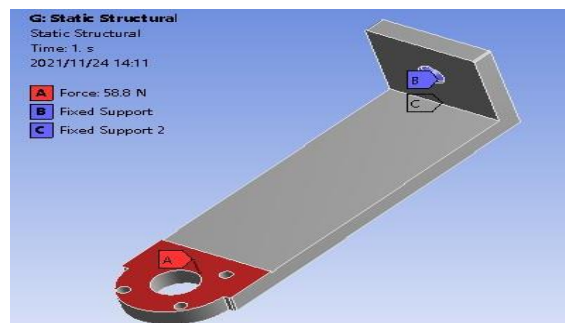


Figure 2-7 Schematic diagram of forearm force

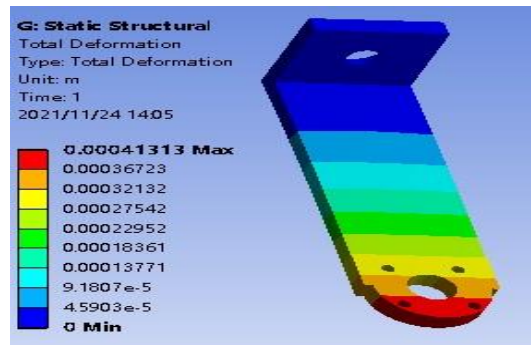


Figure 2-8 Cloud map of overall deformation of the forearm

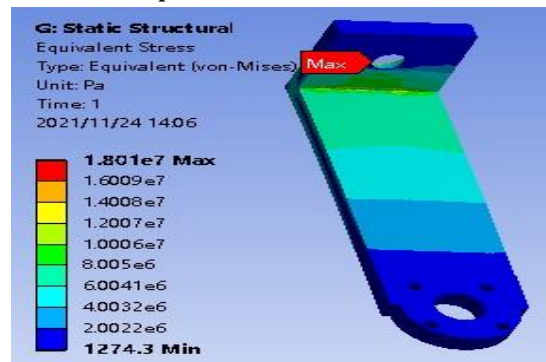


Figure 2-9 Equivalent stress cloud diagram of forearm

According to the simulation analysis results in Figure 2-9, the main deformation of the robotic arm 1 (forearm) is the force-bearing surface A, and its maximum deformation is 0.0004mm. Then according to Figure 2-10, the maximum equivalent stress of the robot arm 1 (small arm) occurs at the edge of the hole, and its maximum equivalent stress is 18MPa, which is less than the yield strength of the aluminum alloy 75MPa. Combined with the analysis of the graph and the results, the robotic arm 1 (small arm) meets the design requirements.

## 4. Robot Kinematics Analysis

### 4.1. Robot space coordinate system

The robotic arm can be regarded as a complete kinematic chain connected by a series of rigid bodies through joints, and these rigid bodies are the rods on the robotic arm. The relationship between the position and posture of the gripper at the end of the manipulator and the base of the manipulator is described by modeling the coordinate system fixed on each link on the manipulator and the relationship between the coordinate systems of each link.

Since the robot has two identical robotic arms, a link mechanism is composed of one robotic arm, the body and the base rotating joint, and the mechanism has two moving joints and four rotating joints. Here, the base of the robot is used as the fixed base coordinate system  $\{0\}$ , which is fixed to the base (ie link 0), and the  $n$ th movable link is link  $n$ , until the link is the end mechanical claw, it is recorded as link  $n + 1$ .

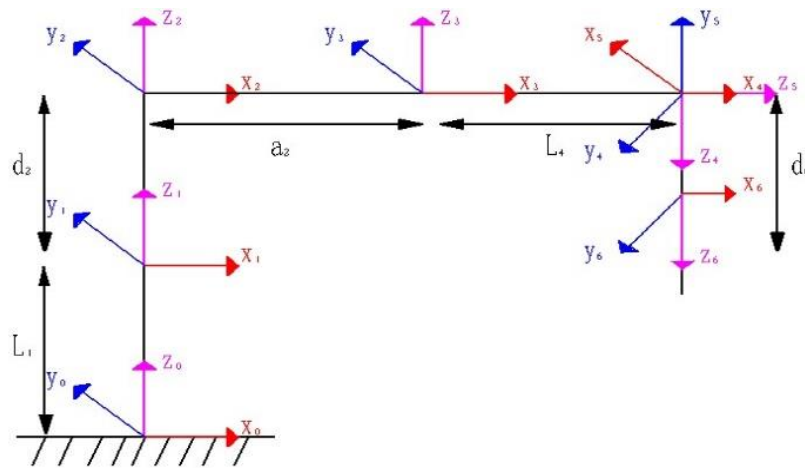


Fig. 4-1 coordinate system of connecting rod of oneside manipulator

As shown in Figure 3-1, the direction of the Zi axis in the connecting rod coordinate system is the direction of the joint axis i; when the joint axis i and i+1 are parallel, the direction of the Xi axis is along the direction of the common perpendicular. When +1 intersects, the direction of the Xi axis is perpendicular to the plane where the two axes intersect, and the direction of the Yi axis is determined by the right-hand rule. According to the established link coordinate system, the D-H parameter table of the manipulator can be obtained, as shown in Table 2.

Table 2 D-H parameter table of unilateral manipulator

$i$	$\alpha_{i-1}$	$a_{i-1}$	$d_i$	$\theta_i$
1	0	0	$L_1$	$\theta_1$
2	0	0	$d_2$	0
3	0	$a_2$	0	$\theta_3$
4	$90^\circ$	0	$L_4$	$\theta_4$
5	$90^\circ$	0	0	$\theta_5$
6	0	0	$d_6$	0

### 4.2. Robot forward and inverse kinematics

According to the transformation law of the link coordinate system in the introduction to robotics, is the general expression of the homogeneous transformation matrix from the th link coordinate system to the th link coordinate system, expressed as:

$${}^{i-1}T_i = \begin{bmatrix} c\theta_i & -s\theta_i & 0 & a_{i-1} \\ s\theta_i c\alpha_{i-1} & c\theta_i c\alpha_{i-1} & -s\alpha_{i-1} & -s\alpha_{i-1}d_i \\ s\theta_i s\alpha_{i-1} & c\theta_i s\alpha_{i-1} & c\alpha_{i-1} & c\alpha_{i-1}d_i \\ 0 & 0 & 0 & 1 \end{bmatrix} \tag{1}$$

In formula 1, c is the abbreviation of cosine function cos; s is the abbreviation of sine function sin.

Substituting the parameters in Table 2 of D-H parameters into Equation 1, the homogeneous transformation matrix of each connecting rod can be obtained as  ${}^0T_1, {}^1T_2, {}^2T_3, {}^3T_4, {}^4T_5, {}^5T_6$ , The homogeneous transformation matrix of the end effector coordinate system {6} relative to the base coordinate system {0} is:

$${}^0T_6 = {}^0T_1 {}^1T_2 {}^2T_3 {}^3T_4 {}^4T_5 {}^5T_6 = \begin{bmatrix} r_{11} & r_{12} & r_{13} & p_x \\ r_{21} & r_{22} & r_{23} & p_y \\ r_{31} & r_{32} & r_{33} & p_z \\ 0 & 0 & 0 & 1 \end{bmatrix} \tag{2}$$

In the formula,  ${}^0T_6$  the elements of are:

$$r_{11} = s_{13}s_5 + c_{13}c_4c_5 \tag{3}$$

$$r_{12} = s_{13}c_4c_5 - c_{13}s_5 \tag{4}$$

$$r_{13} = c_5s_4 \tag{5}$$

$$r_{21} = s_{13}c_5 - c_{13}c_4s_5 \tag{6}$$

$$r_{22} = -c_{13}c_5 - s_{13}c_4s_5 \tag{7}$$

$$r_{23} = -s_4s_5 \tag{8}$$

$$r_{31} = c_{13}s_4 \tag{9}$$

$$r_{32} = s_{13}s_4 \tag{10}$$

$$r_{33} = -c_4 \tag{11}$$

$$p_x = L_4s_{13} + a_2c_1 + d_6c_{13}s_4 \tag{12}$$

$$p_y = -L_4c_{13} + a_2s_1 + d_6s_{13}s_4 \tag{13}$$

$$p_z = d_2 + L_1 - d_6c_4 \tag{14}$$

In the formula, c represents  $\cos\theta$ , s represents  $\sin\theta$ ,  $c_{ij}$  represents  $\cos(\theta_i + \theta_j)$ ,  $s_{ij}$  represents  $\sin(\theta_i + \theta_j)$ .

The inverse kinematics solution of the manipulator is the process of inversely deriving the joint variables of each link joint when the pose of the actuator at the end of the manipulator is known. The end pose equation of the dual-arm robot is:

$${}^0T_6 = \begin{bmatrix} n_x & o_x & a_x & p_x \\ n_y & o_y & a_y & p_y \\ n_z & o_z & a_z & p_z \\ 0 & 0 & 0 & 1 \end{bmatrix} = {}^0T_1(\theta_1) {}^1T_2(d_2) {}^2T_3(\theta_3) {}^3T_4(\theta_4) {}^4T_5(\theta_5) {}^5T_6(d_6) \tag{15}$$

(1) Solving for joint angles  $\theta_4$

Because the end pose equation of the dual-arm robot can be expressed as:

$${}^0T_6 = \begin{bmatrix} n_x & o_x & a_x & p_x \\ n_y & o_y & a_y & p_y \\ n_z & o_z & a_z & p_z \\ 0 & 0 & 0 & 1 \end{bmatrix} = \begin{bmatrix} r_{11} & r_{12} & r_{13} & p_x \\ r_{21} & r_{22} & r_{23} & p_y \\ r_{31} & r_{32} & r_{33} & p_z \\ 0 & 0 & 0 & 1 \end{bmatrix} \tag{16}$$

According to Equation 16, the elements of (3,3) on the left and right sides of the equation are equal to get

$$\theta_4 = \arccos(-a_z) \tag{17}$$

(2) Solving for joint angles  $\theta_5$

According to Equation 16, the elements (1, 3) and (2, 3) on both sides are correspondingly equal, so we can get:

$$\theta_5 = \arctan\left(-\frac{O_z}{n_z}\right) \tag{18}$$

(3) Solving for joint angles  $d_6$

According to the corresponding equality of elements (3, 1) and (3, 2) on both sides of Equation 16, we can get:

$$\frac{a_y}{a_x} = \frac{s_{13}s_4}{c_{13}s_4} \tag{19}$$

Here  $\theta_1 + \theta_3 = \theta$ , available:

$$\theta = \arctan\left(\frac{a_y}{a_x}\right) \tag{20}$$

Then according to Equation 16, the elements (4, 1) and (4, 2) on both sides of the equation are correspondingly equal,

$$p_x = L_4s_{13} + a_2c_1 + d_6c_{13}s_4 \tag{21}$$

$$p_y = -L_4c_{13} + a_2s_1 + d_6s_{13}s_4 \tag{22}$$

Here, the trigonometric functions containing the joint angle are separated, and the formula can be obtained by arranging:

$$\frac{p_x - L_4s_{13}}{a_2} + \frac{-d_6c_{13}s_4}{a_2} = c_1 \tag{23}$$

$$\frac{p_y + L_4c_{13}}{a_2} + \frac{-d_6s_{13}s_4}{a_2} = s_1 \tag{24}$$

In the above formula, in order to make the formula more concise, let  $A_1 = \frac{p_x - L_4s_{13}}{a_2}$ ,  $B_1 = \frac{-c_{13}s_4}{a_2}$ ,

$A_2 = \frac{p_y + L_4c_{13}}{a_2}$ ,  $B_2 = \frac{-s_{13}s_4}{a_2}$ , So equations 23 and 24 can be simplified to get:

$$A_1 + B_1d_6 = c_1 \tag{25}$$

$$A_2 + B_2d_6 = s_1 \tag{26}$$

Then add the left and right squares of Equations 25 and 26 to get:

$$(B_1^2 + B_2^2)d_6^2 + (2A_1B_1 + 2A_2B_2)d_6 + A_1^2 + A_2^2 - 1 = 0 \tag{27}$$

According to Equation 27, it can be obtained  $d_6$ :

$$d_6 = \frac{-(2A_1B_1 + 2A_2B_2) \pm \sqrt{(2A_1B_1 + 2A_2B_2)^2 - 4(B_1^2 + B_2^2)(A_1^2 + A_2^2 - 1)}}{2(B_1^2 + B_2^2)} \tag{28}$$

As can be seen from Equation 28, there are two sets of solutions for the moving joint.

(4) Solving for joint angles  $\theta_1$

According to Equation 25 and Equation 26, it can be obtained:

$$\frac{s_1}{c_1} = \frac{A_2 + B_2d_6}{A_1 + B_1d_6} \tag{29}$$

Solving Equation 29 can get:

$$\theta_1 = \arctan\left(\frac{A_2 + B_2d_6}{A_1 + B_1d_6}\right) \tag{30}$$

(5) Solving for joint angles  $\theta_3$

because  $\theta_1$  a known, The joint angle can be obtained:

$$\theta_3 = \arctan\left(\frac{a_y}{a_x}\right) - \arctan\left(\frac{A_2 + B_2d_6}{A_1 + B_1d_6}\right) \tag{31}$$

(6) Solve for moving joints  $d_2$

According to Equation 16, the elements of (4, 3) on the left and right sides of the equation are equal to get:

$$p_z = d_2 + L_1 - d_6c_4 \tag{32}$$

Because it can be seen from the above that the moving joint and the joint angle have been obtained, and is a fixed value, so the moving joint can be expressed as:

$$d_2 = p_z - L_1 + d_6c_4 \tag{33}$$

## 5. Kinematics Simulation Verification and Trajectory Planning

### 5.1. Robot positive kinematics verification

To verify the correctness of the forward kinematics model of the robot, MATLAB Robotic Tooloxs and analytical methods are usually used for comparison and verification. The D-H parameter table has been established before:  $L_1=150mm$ ,  $L_4=230mm$ ,  $a_2=120mm$ ,

Assign a fixed value to all the joints of the robot:  $\theta_1 = \pi / 2$ ,  $d_2 = 200mm$ ,  $\theta_3 = \pi / 6$ ,  $\theta_4 = \pi / 6$ ,  $\theta_5 = \pi / 2$ ,  $d_6 = 200mm$ .

Substitute the above values into Equation 2 to obtain the pose transformation matrix of the end position as follows:

$${}^0T_6 = \begin{bmatrix} 0.866 & 0.433 & -0.25 & 149.1858 \\ 0.5 & -0.75 & 0.433 & 321.6025 \\ 0 & -0.5 & -0.866 & 176.7949 \\ 0 & 0 & 0 & 1 \end{bmatrix} \tag{33}$$

The correctness of the pose transformation matrix is verified by the MAILAB Robot Toolbox (MATLAB-Robotic Toolbox), and a mathematical model is established in MATLAB. The toolbox's own function "T=fkine(h,q)" can be used to find the derrick climbing robot The pose matrix of the actuator end, the obtained result is consistent with Eq. The established model is as follows:

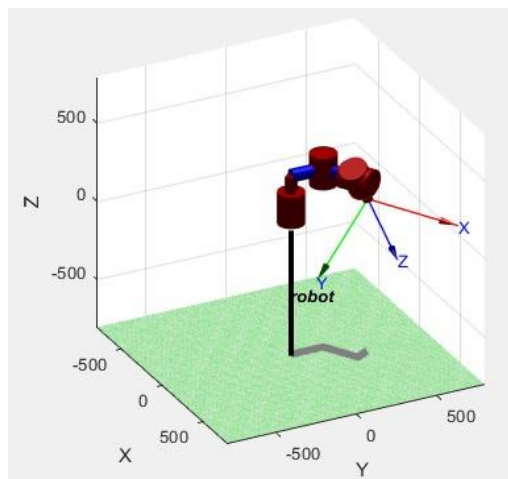


Figure 5-1 3D drawing of the robot model

### 5.2. Robot Inverse Kinematics Verification

In the same way, the verification method of robot inverse kinematics is the same as that of forward kinematics. The value obtained by MATLAB Robotic Toolx toolbox is compared with the value obtained by analytical method [72] to verify the correctness of inverse kinematics.

The values of all joints of the given robot are the same as the joint values of the verified forward kinematics, and then the obtained end pose matrix is substituted into the inverse kinematics equation to obtain two sets of solutions, where the solutions of the first set correspond to the joint space angle values, The correctness of inverse kinematics is proved.

Table 3 Two sets of solutions for inverse kinematics

serial number	joint	Numerical value	joint	Numerical value
1	$\theta_1$	1.571rad	$\theta_4$	0.524 rad
	$d_2$	200 mm	$\theta_5$	1.571 rad
	$\theta_3$	0.524 rad	$d_6$	199.999mm
2	$\theta_1$	-177.382 rad	$\theta_4$	0.524 rad
	$d_2$	22083.852mm	$\theta_5$	1.571 rad
	$\theta_3$	179.476 rad	$d_6$	22084.766 mm

### 5.3. Two-arm space analysis and motion planning simulation

Because the robot designed in this paper is a two-arm robot, if the distance between the arms is not enough, when the two arms of the robot work at the same time, collision and interference may occur between the two arms, which will affect the work safety of the entire robot. Cause damage to the robot and cause property damage. In order to avoid the interference phenomenon of the two manipulators working at the same time, it is necessary to study the two-arm workspace of the robot. The DH parameter table of one arm has been established before. Here, the DH parameter table of the other arm only needs to change  $a_2=-20\text{mm}$ , and other parameters remain unchanged. Establish the initial model of the two-arm robot, where the value of each joint of the robot is:  $\theta_1 = 0, d_2=200\text{mm}, \theta_3 = 0, \theta_4 = 0, \theta_5 = 0, d_6=400\text{mm}$ . The dual-arm robot model established with the MAILAB (MATLAB-Robotic Toolbox) robot toolbox is shown in Figure 4-2 below:

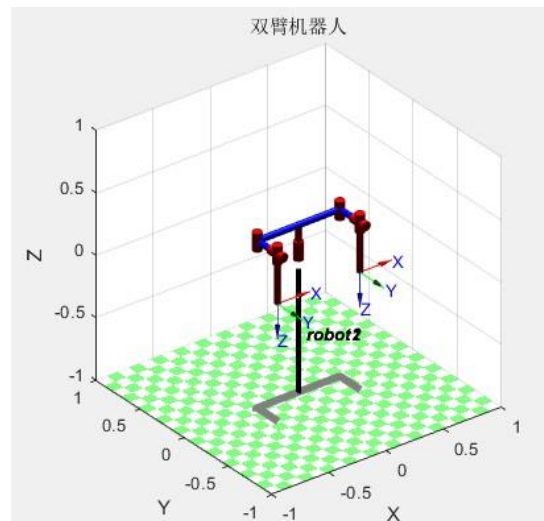


Figure 5-2 3D diagram of the robot arm model

The research on the workspace interference of the two arms of the robot is carried out using the Monte Carlo method, because the base rotation joint of the robot and the lifting mechanism of the fuselage are shared by the two robotic arms, so the above two joints are used in the simulation process. The variation range is set to zero, and the value ranges of the following four joints are substituted into the program for simulation solution. Therefore, when the base rotating joint and the fuselage lifting mechanism do not move, the movable working space of the robotic arm is shown in Figure 4-3:

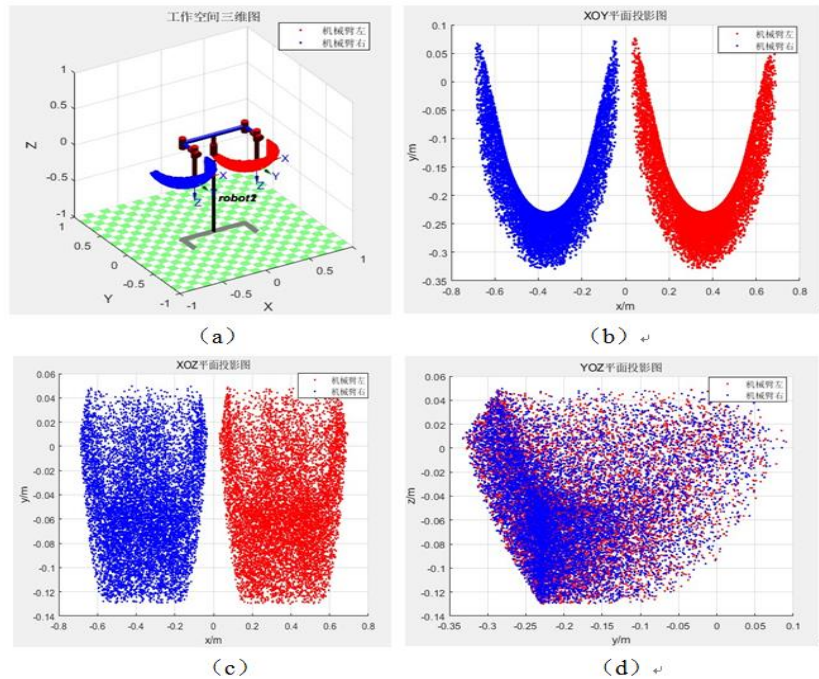


Figure 5-3 The result cloud map of the robot's dual-arm Monte Carlo method

It can be seen from the simulation results in Figure 4-3 that when the two manipulators move at the same time, because the base rotating mechanism and the body lifting structure remain stationary during the simulation process, the movement space range of the manipulator is reduced. However, it can be concluded from (a), (b) and (c) that the two manipulators do not interfere. From the projections of the XOY and XOZ planes, it can be seen that there is a certain difference between the working ranges of the two manipulators. Clearance, thus ensuring the safety of the robotic arm when working. At the same time, it can be seen from the figure (d) that the projections on the YOZ plane have a high degree of overlap between the motion space ranges of the two robots, which indicates that the two robots have good cooperation.

The planning of the motion trajectory is mainly to enable the robot to move smoothly and reduce the phenomenon of emergency stop and rapid acceleration. Here, the robot is set to pass through  $A=(0 \ 54 \ 0 \ \pi/12 \ 0 \ 280)$ ;  $B=(\pi/6 \ 300 \ -\pi/4 \ -\pi/6 \ \pi/3 \ 200)$ ;  $C=(-\pi/2 \ 300 \ -\pi/3 \ \pi/6 \ \pi/4 \ 200)$ ;  $D=(-\pi/2 \ 54 \ 0 \ \pi/6 \ \pi/2 \ 280)$  these four points, in which point A is set as the zero position, and point D is set as the end point. The schematic diagram of the model in four positions is obtained from the plot graphic demonstration:

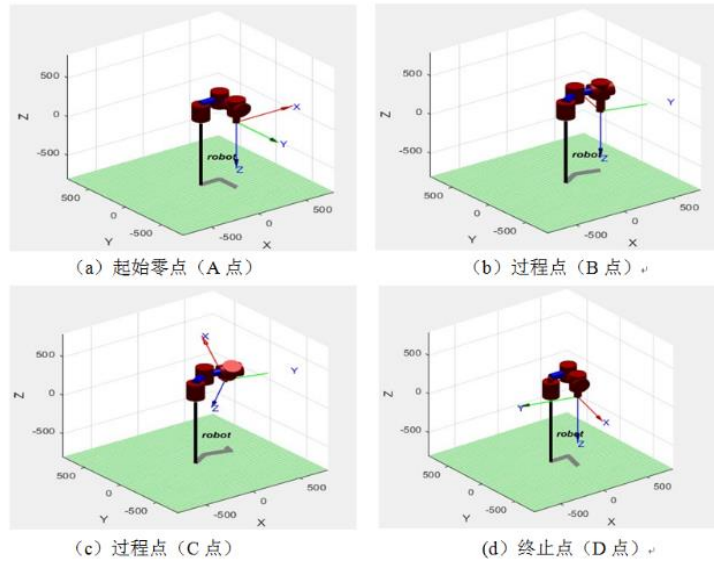


Figure 5-4 Robot motion demonstration

Here, the sampling time from point A to point D is set to 15s, and the change curve of the displacement, velocity, acceleration and trajectory of each joint of the robot over time can be obtained.

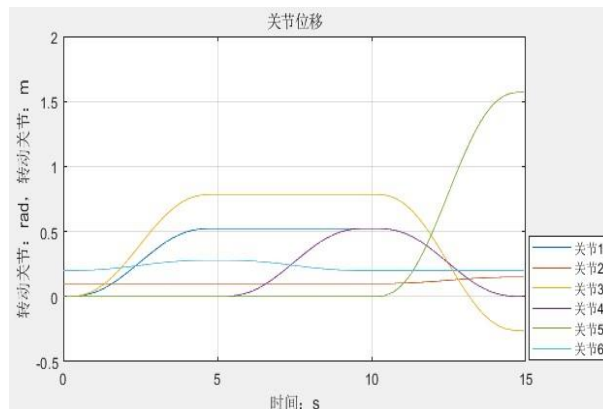


Figure 5-5 Displacement change curve

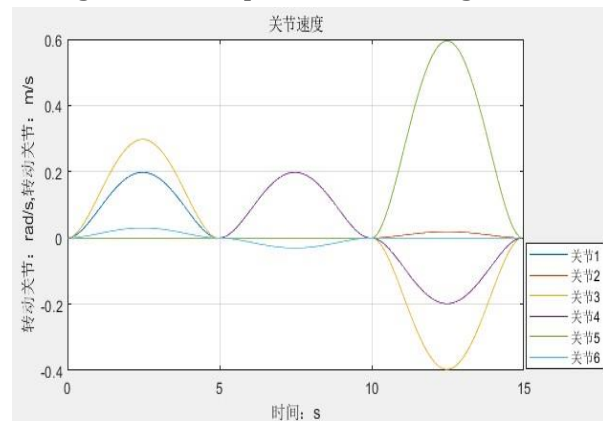


Figure 5-6 Speed change curve

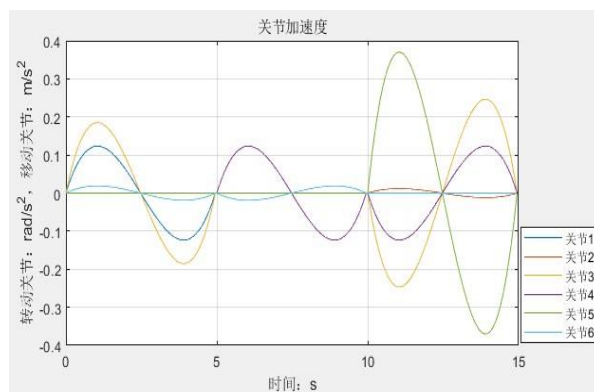


Figure 5-7 Acceleration curve

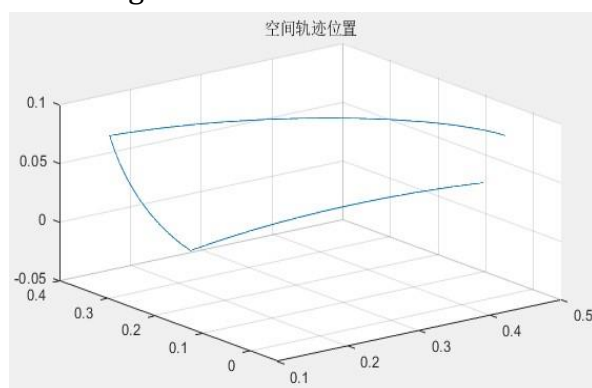


Figure 5-8 Track change curve

It can be seen from Figure 5-7 that the highest requirements for the angular acceleration of the robot's rotary joints are the base rotary joint and the wrist rotary joint, and the two joints are both  $3.927 \text{ rad} / \text{s}^2$ ; The angular velocity requirement is also the highest, the same as  $1.571 \text{ rad} / \text{s}$ . The change curves of the displacement, velocity and acceleration of each joint of the robot with time are relatively smooth and there is no very large mutation.

## 6. Summary

- (1) The finite element static analysis is carried out on the robotic arm, the robotic arm and the ball screw shell of the robot, which ensures the strength of the robotic arm and the ball screw and can be used safely.
- (2) The kinematics of the robot is analyzed, the D-H parameter table is established, and the forward and inverse kinematics mathematical model of the robot is obtained.
- (3) After obtaining the forward and inverse kinematics model of the robot, the correctness of the forward and inverse kinematics of the robot is verified by MATLAB; the workspace of the robot arms is solved by the Monte Carlo method; finally, the trajectory of the robot is calculated. planning to ensure the smoothness of the movement.

## References

- [1]. Borst C, Ott C, Wimbock T, et al. A Humanoid Upper Body System for Two-handed Manipulation[C]// IEEE International Conference on Robotics Automation. IEEE, 2007: 2766-2767.
- [2]. Lemburg J, De G F J, Eich M, et al. AILA – design of an autonomous mobile dual-arm robot[C]. Robotics and Automation (ICRA), 2011 IEEE International Conference on. IEEE, 2011: 5147-5153.
- [3]. Li Xianhua, Tan Shili. A household service robot with two arms and multi-sensor in unstructured environments[C]. International Congress on Image and Signal Processing. Tianjin, China, 2009: 4875-7879.
- [4]. Zhang Yongjie, Xu Hongmei, JAY H Kim, Liu Shuang, Wang Chenglong, Jiang Wei. Finite Element

- Analysis and Topology Optimization of Hammer Feed Milling Rack Plate [J]. Journal of Huazhong Agricultural University, 2019,38(05) :159-167.
- [5]. Zhou Jiping, Yan Jingping, Chen Wenjia. Current Situation and Thinking of Dual-arm Robot Research [M]. Robotics, 2001, 23(2): 175-177.
- [6]. Zhang Kepeng, Qiu Hushan, Deng Chao, Li Kaimin, Liu Xiao, Xing Chao. The application of solidThinking Inspire in the design of automotive leaf spring brackets [J].Automotive Engineer, 2013(10):24-26.
- [7]. Wang Dongshu, Zhu Xunlin. Industrial Robot Technology and Application [M]. China Electric Power Press, 2016.
- [8]. Xue Yuquan. Research on the key technologies of the coordinated operation of the two arms of a service robot [D]. Shanghai University of Applied Sciences, 2020. Wu Weidong, Wang Ste, Wang Xiaodan. Calculation and finite element analysis of hydraulic arm load calculation and finite element analysis [J]. Journal of Heilongjiang University of Science and Technology, 2017, 27(06): 679-684.
- [9]. Xu Jintao. Structural design and motion control of a dual-arm robot [D]. Xidian University, 2019.
- [10].Tian Yong, Wang Hongguang, Pan Xinan, Hu Mingwei. A solution method for the flexibility of collaborative robot workspace [J]. Robotics, 2019, Vol. 41(3): 298-306.
- [11]. Wu Chaoyu, Qian Xiaowu, Yu Wei, Yu Jin. Workspace Analysis and Optimization of Linear Drive Parallel Robot [J]. Journal of Agricultural Machinery, 2018, Vol. 49(1): 381-389.